Experimental Validation and Calibration of GNSS-Based Phase Synchronization for Bistatic and Multistatic SAR Missions

Eduardo Rodrigues-Silva, *Graduate Student Member, IEEE*, Marc Rodriguez-Cassola, Alberto Moreira, *Fellow, IEEE*, and Gerhard Krieger, *Fellow, IEEE*

***Abstract*— This article addresses the critical issue of phase synchronization in multistatic synthetic aperture radar (SAR). We present the experimental validation of a global navigation satellite system (GNSS)-based synchronization technique planned for use in ESA's upcoming Earth Explorer mission, Harmony. In this technique, the radar payload and GNSS receiver utilize the same main oscillator, and radar synchronization is achieved through the postprocessing of carrier phase data from the GNSS receiver and precise baseline determination (PBD) outputs. This article presents an experimental procedure that serves as a general proof of concept of the technique, a method for assessing the achievable synchronization accuracy for a given GNSS receiver, and a method to estimate the covariance matrix to optimize the weighting between the various carrier phase observables. We present point-to-point estimation and smoothing approaches. The technique achieved in a laboratory environment relative synchronization errors below 515 fs (1σ), or 1° for a 5.4-GHz radar system, in a zero-baseline scenario, and below 1.5° at 5.4 GHz in a short-baseline scenario, in which the systems are physically separated.**

***Index Terms*— Bistatic radar, calibration algorithms, multistatic radar, performance analysis, time and phase synchronization.**

I. Introduction

FOLLOWING the trend toward small satellites, many bistatic and multistatic spaceborne synthetic aperture radar (SAR) concepts have been proposed, such as the ones described in [1], [2], [3], [4], and [5]. All of those concepts depend on accurate synchronization of the radar payloads, which, in general, presents one of the most critical challenges in bistatic and multistatic SAR systems. In addition, the potential benefits that add-on missions such as the planned ESA's Earth Explorer Harmony mission may offer in the future highlight the need for standardization in synchronization solutions.

Very few bistatic systems have been successfully demonstrated in space. The pioneer in demonstrating bistatic operations on separate platforms was TanDEM-X [6], [7], which achieved unparalleled digital elevation models (DEMs) accuracy. TanDEM-X required the knowledge of relative phases within a few degrees to avoid systematic modulations in the measurements, which is a typical requirement for interferometric products [8], [9]. More recently, the LuTan-1 bistatic mission successfully demonstrated the operation of a bistatic SAR system in the L-band. Both missions relied on synchronization links [10], [11], which could be too costly, complex, or even unfeasible on system concepts using three or more satellites.

The use of global navigation satellite systems (GNSSs) for synchronization is well established [12], and it has also been proposed for radar applications. Wang et al. [13] propose using GNSS receivers to synchronize spaceborne bistatic radar systems by disciplining the radar oscillator of the radar payloads with the GNSS pulse per second (PPS) signals. The proposed technique considerably reduces the differential phase drifts but relies on data-based approaches to reduce the remaining residuals to acceptable levels. Similarly, Sandenbergh et al. [14] propose and evaluate a GNSS-based synchronization technique for a ground-based tristatic pulsed-Doppler networked radar system using GPS-disciplined oscillators. Good performance for the proposed application was reported, with a maximum measured phase slope of −92°/s, but the same performance is far from sufficient for more stringent applications such as distributed SAR imaging and interferometry.

Rodrigues-Silva et al. [15] proposed a GNSS-based phase synchronization technique based on the common-view carrier phase measurements in which the radar payload and the GNSS receiver share the same main oscillator. This synchronization concept requires only precise baseline determination (PBD), which is already required for most use cases of bistatic and multistatic systems. The technique is easy to implement in hardware and does not require any signal exchange between the satellites, making it an ideal synchronization solution in terms of simplicity, scalability, and ease of integration between different systems. The concept was selected as the nominal synchronization technique for the Harmony mission [16].

The Harmony mission consists of two lightweight companion satellites to the Sentinel-1 spacecraft, with receive-only radars as main payloads. The mission has diverse scientific objectives, including the observation and quantification of small-scale motion and deformation fields at the air–sea interface, the solid Earth, and the cryosphere [17]. The mission will alternate between two configurations: one in which the two satellites are separated by hundreds of kilometers and another where the satellites fly in close formation. The latter configuration will be used for cross-track interferometry

Received 14 November 2024; revised 14 February 2025; accepted 23 March 2025. Date of publication 15 April 2025; date of current version 21 April 2025. The work was supported by the DLR-DAAD Research Fellowship Programme. *(Corresponding author: Eduardo Rodrigues-Silva.)*

The authors are with the Microwaves and Radar Institute, German Aerospace Center (DLR), Oberpfaffenhofen, 82234 Weßling, Germany (e-mail: eduardo.rodriguessilvafilho@dlr.de).

Digital Object Identifier 10.1109/TGRS.2025.3557151

and will require highly accurate phase synchronization, proportional to the specific application requirements. In this case, two bistatic Harmony SAR images will be compared. Since the synchronization error contribution from Sentinel-1 mainly cancels out in the interferograms, only synchronization between the two Harmony satellites will be needed, similar to conventional single-pass interferometric missions. The work presented in this article applies to both conventional missions and companion mission concepts such as Harmony.

In this article, we present a proof of concept of the technique proposed in [15] and investigate the conditions under which it can achieve high accuracy with commercial GNSS receivers, being a direct complement to the aforementioned publication. We isolate the clock contamination within the tested receivers in a laboratory environment. This contamination causes a common error signal that cannot be reduced through averaging and, therefore, represents a performance limitation of the technique. We present a way of characterizing this contamination by estimating the covariance matrix of the motion-compensated carrier phase observables set. Then, we use this matrix to obtain near-optimal weighting. Most importantly, we demonstrate that the technique can achieve high synchronization accuracy with current GNSS technology in a lab environment, assuming that the previously identified error contributions [15], mainly multipath and crosstalk, are either suppressed or corrected.

This article is organized as follows. In Section II, we explain the GNSS-based synchronization technique in general terms and the critical error sources. In Section III, we describe the experimental methods and hardware setup. In Section IV, we present a method to calibrate the estimation algorithm. In Section V, we present the experimental results and assess the achievable accuracy of the technique with different GNSS receivers. In Section VI, we summarize the conclusions of the experiments.

II. GNSS-Based Phase Synchronization

A. Technique Description

Fig. 1 illustrates the fundamental hardware architecture required for GNSS-based synchronization. In this proposed design, a single ultrastable oscillator (USO) generates the radar carrier and the reference signals within the GNSS receiver. The received GNSS signal undergoes downconversion and is then compared to internally generated GNSS code and carrier signals at an intermediate frequency. The receiver generates the signal for downconversion and the reference GNSS signal coherently from the main oscillator.

In this configuration, the carrier phase measurement difference between the two platforms $L_{uv,k}^{(i)}$ (in units of meters), known as single-difference carrier phase observable, contains information about the range variation between the GNSS receiver and transmitter, and differences in clock drifts, as expressed in

$$L_{uv,k}^{(i)}(t) = \rho_{uv}^{(i)}(t) + \mathrm{c} \cdot \delta t_{uv}(t) - \left(\frac{\lambda_k}{\lambda_1}\right)^2 \cdot I_{uv}^{(i)}(t) - \lambda_k \cdot A_{uv,k}^{(i)} + M_{uv,k}^{(i)}(t) + \frac{\lambda_k}{2\pi} \cdot \delta\psi_{\mathrm{hw},k} + v_{n,k}^{(i)}(t) \quad (1)$$

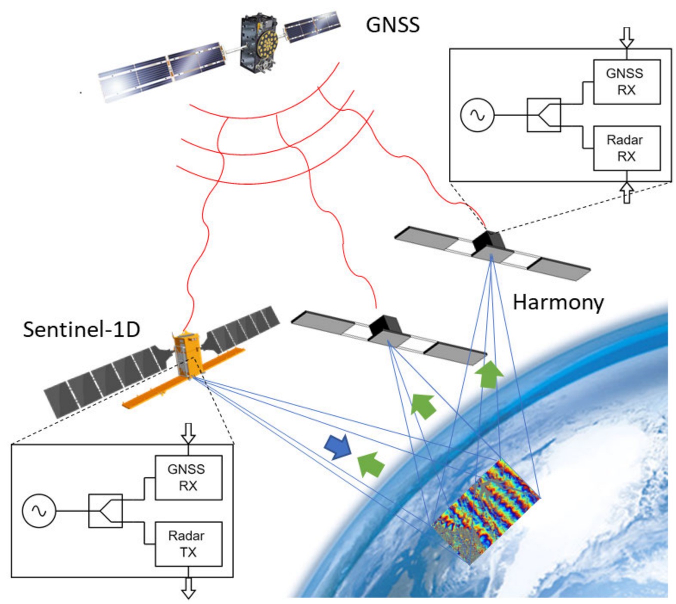

Fig. 1. GNSS-based phase synchronization scheme (satellite model credits: ESA). Sentinel-1D is the main TX/Rx SAR satellite, whereas Harmony consists of two receive-only satellites building a multistatic SAR system [16].

where $\rho_{uv}^{(i)}$ is the difference between the distances from receivers v and u to the ith navigation satellite, c is the speed of light in vacuum, δt_{uv} is the differential clock bias, $I_{uv}^{(i)}$ is the difference between the biases caused by the ionospheric delays for a signal at wavelength λ_1, $A_{uv,k}^{(i)}$ is the difference between ambiguities, $M_{uv,k}^{(i)}(t)$ describes other systematic error components including multipath, crosstalk, tracking channel bias, and phase wind-up, $\delta\psi_{\mathrm{hw},k}$ denotes a residual signal-dependent signature originating in the navigation receiver, and $v_{n,k}^{(i)}(t)$ is residual error component, including thermal noise.[1] The term $\delta\psi_{\mathrm{hw},k}$ represents a broad component that accounts for the empirically observed error common to all signals of a given type. This error may or may not be correlated between signals and includes hardware-related residuals and potential processing artifacts.

From (1), a biased estimate of the reference phase difference at the radar carrier frequency $\tilde{\psi}_{0,k}^{(i)}$ can be obtained from this measurement by isolating the clock term using estimates of the differential range $\tilde{\rho}_{uv}^{(i)}$ and the differential ionospheric delay $\tilde{I}_{uv}^{(i)}$ at wavelength λ_1 as follows:

$$\tilde{\psi}_{0,k}^{(i)} = \frac{2\pi}{\lambda_0} \cdot \left[L_{uv,k}^{(i)} - \tilde{\rho}_{uv}^{(i)} + \left(\frac{\lambda_k}{\lambda_1}\right)^2 \cdot \tilde{I}_{uv}^{(i)}\right] \quad (2)$$

where λ_0 is the radar carrier wavelength. Ignoring the constant biases and time-varying components of PBD and differential ionospheric delay estimation, the time-varying tracking error

[1]We denote, in this article, the upper index $()^{(i)}$ as relating to the GNSS satellite i, the lower indexes $()_u$ and $()_v$ as relating to the receivers in the satellites u and v, and the lower index followed by a comma, as in $()_{u,k}$, as related to the reference frequency, with navigation carrier frequency denoted by k, and the radar carrier by 0. Furthermore, we denote the difference between quantities as $()_{uv} = ()_v - ()_u$.

$\epsilon_{uv,k}^{(i)}$ of the individual estimate is given by

$$\epsilon_{uv,k}^{(i)} = \frac{2\pi}{\lambda_0} \cdot M_{uv,k}^{(i)} + \frac{\lambda_k}{\lambda_0} \cdot \delta\psi_{\mathrm{hw},k} + \frac{2\pi}{\lambda_0} \cdot \upsilon_{n,k}^{(i)}. \tag{3}$$

The following biased estimate of the phase difference between the oscillators' signals over time at the carrier frequency can be derived from this measurement model [15]:

$$\tilde{\psi}_{uv,0} = \sum_{i=1}^{N} \sum_{k=1}^{n_\lambda^{(i)}} \alpha_k^{(i)} \cdot \tilde{\psi}_{0,k}^{(i)} \tag{4}$$

where $\alpha_k^{(i)}$ are weighting factors, N is the number of GNSS satellites, and $n_\lambda^{(i)}$ is the number of signals transmitted by GNSS satellite i. Only GNSS data acquired continuously during the whole acquisition period are used.

Defining the model matrix A as a matrix of one column and the number of lines equal to the number of carrier phase observables $n_{\mathrm{cp}} = \sum_{i=1}^{N} n_\lambda^{(i)}$

$$A = [1 \quad 1 \quad \cdots \quad 1]_{1\times n_{\mathrm{cp}}}^{\mathrm{T}} \tag{5}$$

the optimal set of weights in a least-squares sense is given by

$$\mathrm{W} = \left[\alpha_k^{(i)}\right]_{1\times n_{\mathrm{cp}}} = \left(A^T \cdot S^{-1} \cdot A\right)^{-1} \cdot A^T \cdot S^{-1} \tag{6}$$

in which S is the covariance matrix of the set of carrier phase observables

$$S_{kl}^{(ij)} = \mathrm{Cov}\left(\epsilon_{uv,k}^{(i)}, \epsilon_{uv,l}^{(j)}\right) \tag{7}$$

where l also denotes a reference GNSS frequency.

Although the estimation algorithm is developed under ideal assumptions, it is crucial to evaluate the impact of deviations from these ideal models. The geometric terms, ionosphere, and ambiguities are thoroughly analyzed in [15], which also explains how the technique can employ ionosphere-free linear combinations when the ionosphere's time-varying effects are significant. However, this scenario is unlikely for short distances below 1 km and is certainly not applicable to the experiments with physical antennas and real GNSS signals presented in this article. Based on prior research and simulations, in that article, we concluded that state-of-the-art baseline determination and GNSS satellite positioning are precise enough to ensure that geometry-related terms do not substantially contribute to the synchronization error budget in the time frame of a few minutes.

The geometric terms, as stated previously, should be derived from POD, utilizing algorithms such as those detailed in [18]. Accurate GNSS satellite positions can be obtained from various International GNSS Service (IGS) and Multi-GNSS Experiment (MGEX) analysis centers, which provide precise position data through public archives with a posteriori accuracy below the decimeter level [19]. For short baselines spanning only a few meters, such as those used in the short-baseline experiments presented further in this article, the GNSS position errors effectively cancel out. As a result, the inaccuracies introduced can be safely disregarded, even when using the less precise broadcast ephemerides.

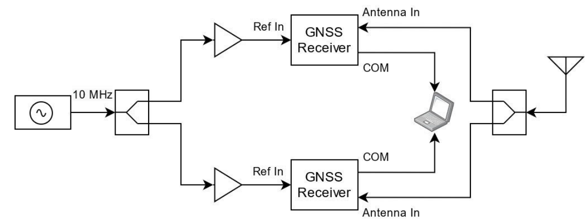

Fig. 2. Common-oscillator, zero-baseline experimental setup.

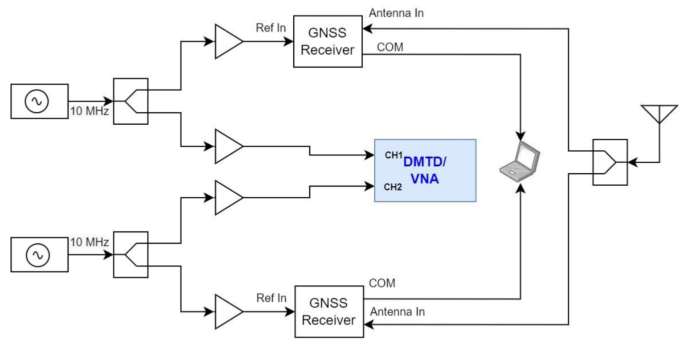

Fig. 3. Two-oscillator, zero-baseline experiment setup.

B. Issue of Clock Contamination

In conventional navigation applications, the internal clock in a GNSS receiver is, by default, filtered and steered to match the GPS time, minimizing the clock offset estimated in the navigation solution. This means that the coherence between the internal receiver reference and the external oscillator is usually lost by default. The receiver tracking performance is specified in terms of the thermal noise, which does not include any clock tracking error. In summary, a high coherence between internal and external frequency references is usually unnecessary. Therefore, we cannot expect conventional receivers to be designed to fulfill the level of accuracy necessary for SAR synchronization. Needless to say, the aforementioned clock steering has to be disabled in case the receiver is used for synchronization in the way described in this article.

The coherence between the external reference and the internal reference GNSS signals can be determined by calculating the single differences of the carrier phase measurements between two receivers taking as input the same GNSS signal (e.g., using the same antenna) and the same main oscillator, as illustrated in Fig. 2. Results from such experiments are reported in [20], where the authors show a higher standard deviation from the carrier phase single differences than expected from the specifications. This indicates a contamination of the reference phase within the receiver.

These phase errors introduced within the GNSS receivers could dominate the phase error budget for bistatic SAR and still have little impact on most conventional GNSS applications. The technique here presented relies on averaging the carrier phase observables to reduce the synchronization error. In case there is a noise component common to all observables, it will not be reduced through averaging, and this common component will become a performance limiter. Therefore, a better understanding of the reference tracking capability of

GNSS receivers is necessary for assessing the technique's full potential.

C. Remarks on Time Synchronization

Time synchronization in multistatic and bistatic radars involves the precise timing of individual pulse reception to ensure correct range bin alignment and full recording of echo signals. Although this article focuses on phase synchronization, which is arguably the most challenging synchronization problem, the hardware configuration required for the proposed technique also enables time synchronization. In this setup, the receiver hardware is coherent with the GNSS timing system, allowing individual received signal samples to be time-tagged with GNSS timing precision, typically below 50 ns for real-time position, velocity, and time (PVT) solutions and potentially below 1 ns with POD solutions [21].

Furthermore, the time difference between transmission and reception can be tracked with much greater accuracy using the phase synchronization solution itself. Due to the coherence between the generated carrier and timing signals, time and phase differences are directly proportional to each other. As a result, the transmission-reception time difference could, in principle, be determined a posteriori according to the results presented in Section V, which, in terms of time, corresponds to a few picoseconds or less, provided that hardware delays are calibrated. This approach resembles the solution employed in TanDEM-X, where a PPS generated by the radar oscillator is compared with PPS signals from the GNSS receiver, and the resulting difference is used to compensate for the echo window drift of the receiving radar system [8].

III. Experimental Method

A. Hardware Setup

Figs. 2–4 illustrate the experimental setups used. The sequence of experiments is designed so that the expected error factors are introduced gradually, and more terms are taken into account at each iteration. Three different receivers were used: the development kit of the OEM729 manufactured by Novatel, which is a product aimed at mass production for a broad range of applications [22]; the PolaRx5TR receiver manufactured by Septentrio, more specialized equipment targeted at high-performance time-transfer and geodetic applications [23]; and the space-grade PODRIX receivers, a high-end radiation hardened receiver manufactured by Beyond Gravity, which has been used in several missions for precise orbit determination [24] and time synchronization [25]. The receivers are powered on for at least two hours before each experiment, a time empirically verified to be sufficient for the receivers to reach thermal equilibrium. The frequency of the external oscillators under analysis driving the GNSS receivers was adjusted to be well below 0.2 Hz difference from one another through their respective command interfaces. We observed that above this threshold, the frequency offset introduces errors on the clock term of the carrier phase that could not be distinguished from the phase noise signature of the oscillators.

For the short-baseline experiments illustrated in Fig. 4, the differential range histories from GNSS satellites to the fixed

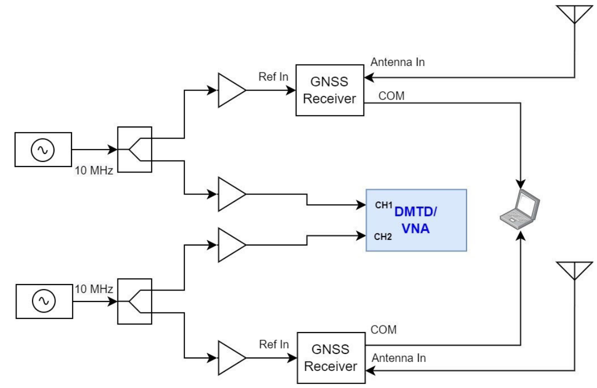

Fig. 4. Two-oscillator, short-baseline experiment setup.

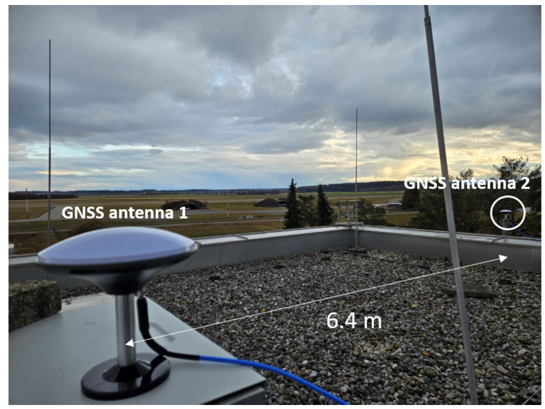

Fig. 5. Antenna placement in the experiments with the PolaRx5TR receivers on the roof of a building at DLR campus in Oberpfaffenhofen.

antennas are used to calibrate the carrier phase measurements, as indicated in (2). Fig. 5 shows the antenna placement for those experiments. The employed antenna has no multipath suppression, and despite it being a calibrated product for geodetic applications, we can expect considerable contamination from reflections from the ground.

Fig. 6 shows the test setup assembled as a proof of concept for orbital scenarios and a preliminary assessment of the phase tracking performance of the PODRIX receivers under simulated orbital conditions. The high-end GSS9000 GNSS signal simulator from Spirent was used to generate the signals received in a formation flying scenario for a Sun-synchronous orbit at 700-km altitude and baselines of the order of 400 m in a helix-like orbit formation. This simulator has been previously used for testing POD applications for LEO orbits [26], [27]. The PODRIX receivers are planned to be used in the Harmony mission for precise orbit determination and synchronization.

In the experiment discussed in this article, we simulated neither ionospheric delays, which are estimated to be negligible, nor multipath, which largely depends on the spacecraft shape and antenna placement. These error contributions under orbital scenarios are discussed in detail in [15] based on previous publications in the field of POD.

This experiment with the PODRIX receivers also serves as a proof of concept for an orbital scenario for the GNSS-based phase synchronization technique, as it employs, for the first time, space-grade hardware and simulated GNSS signals with Doppler and baselines representative of satellite formation flying conditions. The clock contamination mentioned in

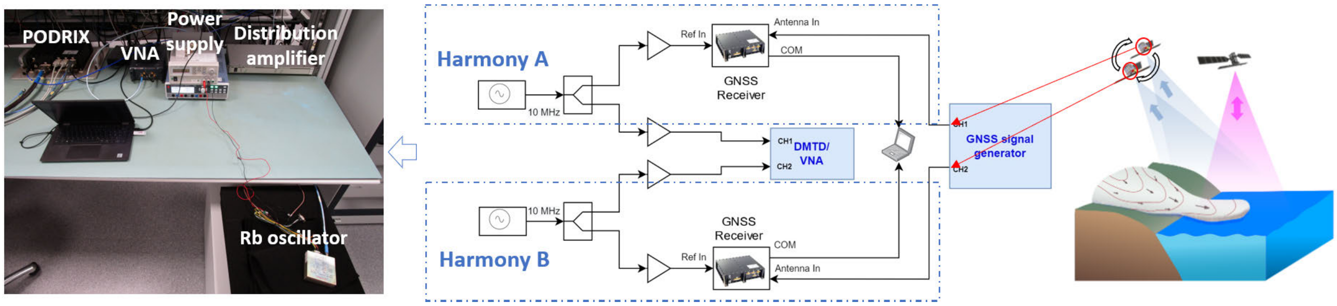

Fig. 6. Two-oscillator, simulated formation flying validation setup. The receive-only satellites are defined as Harmony A and Harmony B. The Harmony formation illustration on the right was adapted from [17].

Section II-B could be coming from GNSS processing residual correlations or be a hardware effect sensitive to the central frequency of the incoming signal. Therefore, we consider that it is necessary to verify if the conditions leading to this contamination of the clock term are not aggravated by a much higher and fast-changing Doppler difference between the GNSS receivers seen in an orbital scenario.

Finally, it is important to emphasize that none of the GNSS receivers used in the tests were modified or customized in any way; all were standard commercial off-the-shelf equipment.

B. Reference Synchronization Rate and Reference Bandwidth Determination

A boundary for the estimation rate of the clock phase differences can be derived based on data collected with a TanDEM-X calibration data take. The data consist of synchronization pulses only, exchanged at a rate of around 3 kHz, which allows a proper sampling of the phase noise spectrum of the two oscillators. The data have been scaled from the carrier frequency of TerraSAR-X to the carrier frequency of Sentinel-1, and the spectral shape has been maintained. The underlying assumption for the validity of the presented results is that the TanDEM-X main oscillators have similar phase noise characteristics to both the Sentinel-1 and Harmony oscillators. Because measurements with more representative oscillators are unavailable, the TanDEM-X case represents the best approximation for an operational scenario.

Fig. 7 shows the reconstruction error after downsampling the data to different rates. The plot shows that an estimation rate of 2 Hz seems to capture most of the energy of the phase noise spectrum. This suggests that an estimation rate between 1 and 2 Hz might be sufficient for a C-band Harmony case with oscillators of similar quality to those of TanDEM-X. We will use an estimation rate of 2 Hz as a reference in the evaluations presented in this article.

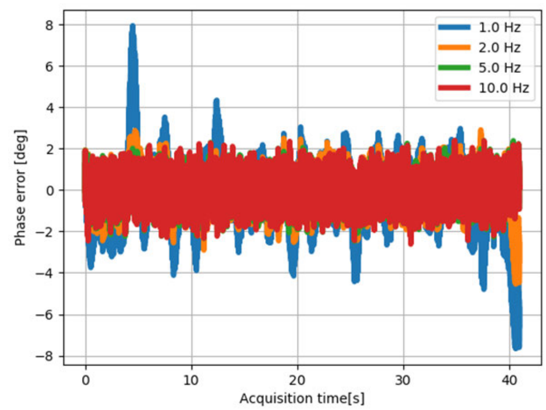

Fig. 7. Reconstruction error after downsampling-then-interpolating TanDEM-X synchronization data with different rates.

C. Differential Phase Ground-Truth Comparison

The so-called dual-mixer time-difference (DMTD) method, implemented in the phase noise analyzers, is conventionally used to compare references very close to each other (e.g., a difference of much less than 1 Hz for a 10-MHz reference) and is reported to achieve accuracy of a few hundred, or even a few tens, of femtoseconds. Vector network analyzers (VNAs) can also measure the phase of an incoming signal with respect to an internal or external reference. A high-accuracy phase measurement can be obtained analogously to the DMTD method by comparing two input signals with the same reference.

For all the experiments in which two independent frequency references are used, the phase between the oscillators is measured simultaneously by using an independent device. Fig. 8 describes the overall measurement setup for those cases. The device is configured for a bandwidth of 100 Hz, which can capture the variations of the phase difference between the 10-MHz oscillators. In each data take, the direct relative phase data acquisition begins before the acquisition with GNSS and ends after the acquisition with GNSS. The reference is undersampled to match the sampling rate of the GNSS data and correlated until the peak is found to allow for the alignment of the two independent measurements. The undersampling is done for all the possible data combinations, and the maximum correlation dataset is selected. Finally, the data obtained through GNSS and the independent instrument are compared, and the estimation errors are calculated. The reference relative measurement phase is obtained using the VNA P5024A during the experiment.

A moving average filter is applied to the reference to emulate the effect of the SAR processing on the phase noise of the data.

D. Remarks on the Synchronization Time Scales

The experiments presented in this article span from a few tens of seconds to a few minutes. The fact that they

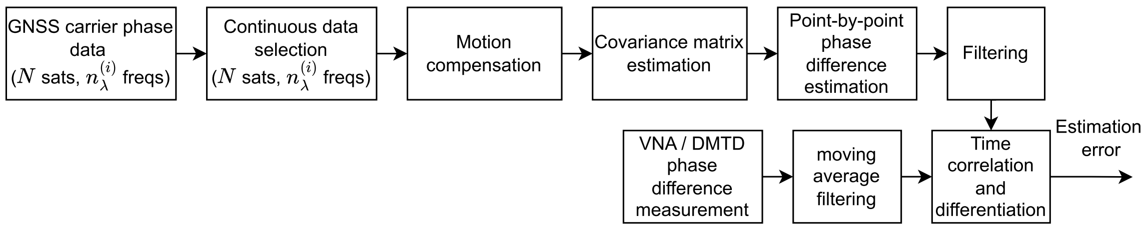

Fig. 8. Data processing chain and comparison to reference.

capture only a limited number of GNSS geometry instances, however, does not compromise the generality of the proof of concept. The technique relies on POD to compensate for relative motion, which involves usually fitting a highly accurate dynamic model to GNSS data over multiple orbits with varied visibility geometry. Consequently, unlike in conventional PVT applications, the instantaneous geometry does not directly influence the instantaneous estimation. Instead, the differential phase estimation is driven by the number of tracked signals of sufficient quality, i.e., those with sufficiently high elevation. The number of satellites in view is expected to consistently exceed seven for each major constellation [28]. In the case of multifrequency, multiconstellation receivers—which are recommended for this application—the number of tracked signals is likely constrained by the GNSS receiver's number of available channels rather than the local geometry.

In conclusion, we do not expect the GNSS variability to cause a performance discrepancy that would hinder the technique's overall usability. This is supported by our analysis and experiments, and the consistency of results presented in this article across various hardware configurations.

From the perspective of bistatic and multistatic SAR applications, phase synchronization needs to be ensured in the time scales slightly below the synthetic aperture and within the acquisition, which usually is in the order of minutes. The results presented in this article consist of short-duration data takes, separated by hours or days, with durations exceeding that of conventional synthetic apertures and being representative of typical interferometric acquisitions. For longer data takes lasting tens of minutes, for example, performance may degrade, potentially becoming dominated by factors such as slow temperature variations and the accuracy of precise orbit determination.

The applicability of the technique for long-term accurate phase tracking could be useful in an operational scenario to obtain, for example, consistent absolute phase referencing. For that case, a piecewise estimation could be thought of, which would only require the estimation of a constant offset between the pieces, something that can be easily done using data-based approaches [29]. Events degrading suddenly the estimations (e.g., bubbles in the ionosphere, rebooting of the receivers, and signal fadings) are unlikely to happen, but, even if they do happen, they are expected to represent just eventual loss of a data take.

As a last remark, note that, in principle, the technique here evaluated can continuously track phase as long as GNSS signals are available and unaffected by outages caused by factors such as jamming or other interferences.

IV. Calibration and Filtering

A. Covariance Matrix Measurement

The receiver-induced error calibration procedure proposed here is based on the same-oscillator, zero-baseline setup illustrated in Fig. 2. Most of the terms in the differential carrier phase expressed in (1) cancel out in this setup. In an ideal case, the differential carrier phase obtained in this experiment would consist of a constant signal plus a noise component in line with the thermal noise specification of the receiver. However, we observed that the noise level of the differential carrier phase experiment is above the specifications, and in addition, the errors are correlated for different carrier phase measurements. This correlation depends mainly on the type of signal being tracked but is independent of the GNSS satellites from which it originates. Therefore, we model it as an error component common to signals of the same type, denoted $\delta\psi_{\mathrm{hw},k}$, in the carrier phase observable model (1).

Assuming the thermal noise and multipath components in the error model (3) uncorrelated, the covariance matrix's off-diagonal terms (i.e., S_{kl}^{ij} in which $i \neq j$ or $k \neq l$) are given by

$$S_{kl}^{ij} = \mathrm{Cov}\left(\frac{\lambda_k}{\lambda_0} \cdot \delta\psi_{\mathrm{hw},k}, \frac{\lambda_l}{\lambda_0} \cdot \delta\psi_{\mathrm{hw},l}\right). \tag{8}$$

Assuming that the thermal noise is uncorrelated across channels, we can obtain an estimate of the off-diagonal terms of S by averaging the correlations of zero-baseline, same-oscillator carrier phase measurements, as shown in the following equations.

For $k \neq l$

$$S_{kl}^{ij} = \frac{1}{N_k \cdot N_l} \cdot \sum_{i=1}^{N_k} \sum_{j=1}^{N_l} \mathrm{Cov}\left(\tilde{\psi}_{0,k}^{(i)}, \tilde{\psi}_{0,l}^{(j)}\right). \tag{9}$$

For $k = l$

$$S_{kl}^{ij} = \frac{1}{N_k \cdot N_l - 1} \cdot \sum_{i=1}^{N_k} \sum_{j=1}^{N_l} (1 - \delta_{ij}) \cdot \mathrm{Cov}\left(\tilde{\psi}_{0,k}^{(i)}, \tilde{\psi}_{0,l}^{(j)}\right) \tag{10}$$

where N_k and N_l are the number of GNSS satellites in view transmitting the frequency k and l, respectively, and δ_{ij} is the Kronecker delta, equal to 1 when $i = j$ and 0 otherwise.

In the following, we need to determine the matrix's diagonal terms, which correspond to the error variance in each carrier phase measurement. Unlike the off-diagonals, the diagonal terms are highly dependent on circumstantial factors, such as elevation and multipath. In principle, they cannot be accurately predicted a priori and must be inferred from the individual data take.

Defining the motion compensated and scaled double differences $\mathrm{DD}_{kl}^{(ij)}$ as

$$\mathrm{DD}_{kl}^{(ij)} = \tilde{\psi}_{0,k}^{(i)} - \tilde{\psi}_{0,l}^{(j)} \tag{11}$$

we can derive from (3)

$$\mathrm{Var}\left(\epsilon_{\mathrm{uv,k}}^{(\mathrm{i})}\right) + \mathrm{Var}\left(\epsilon_{\mathrm{uv,l}}^{(\mathrm{j})}\right) = \mathrm{Var}\left(\mathrm{DD}_{kl}^{(ij)}\right) + 2 \cdot S_{kl}^{ij}. \tag{12}$$

The terms on the left correspond to two distinct diagonal elements of the covariance matrix S, which we would like to estimate. The term $\mathrm{Var}(\mathrm{DD}_{kl}^{(ij)})$ can be computed from the carrier phase dataset that will be used to estimate the differential phase noise. The term S_{kl}^{ij} can be replaced by the previously calibrated off-diagonal terms from a zero-baseline experiment. Applying (12) to all possible combinations of signals, i.e., for all i, j, k, and l, with $i \neq j$ or $k \neq l$, results in a linear overdetermined system of equations, which can be solved using simple least-squares estimation. Note that the least-squared estimator already yields good results when assigning uniform weights to each equation, but there is still potential to improve it by including a nonidentity weight matrix.

The effectiveness of the estimation can be assessed in a two-oscillator, zero-baseline experiment, where the covariance matrix can be directly measured. Fig. 9 shows the estimated covariance matrix and the estimation error. Different datasets were used to calibrate the covariance matrix and test the technique. The good conformance between estimated and measured covariance matrices demonstrates that the approach here presented is able to characterize the variances and covariances of a given set of differential carrier phase observables.

One implicit assumption is that the variance of the common mode remains constant for both the calibration set and the use case. This implies that any environmental factors influencing the common mode, particularly thermal conditions, must be kept stable. In an orbital scenario, the covariance may need to be reassessed as part of in-orbit testing routines, potentially requiring an external reference. This could be achieved, for instance, through autosynchronization on specific, well-characterized scenes [29].

Finally, it is worth noting that the possibility of completely avoiding the common mode cannot be ruled out if greater control over receiver hardware is available. In this work, we present a procedure that significantly improves results from the user's perspective, while receiver design considerations remain outside the scope of this article. Since the common mode is a key performance factor for the proposed technique, a more detailed future analysis of the GNSS receiver characteristics or the signal properties contributing to this common mode is necessary.

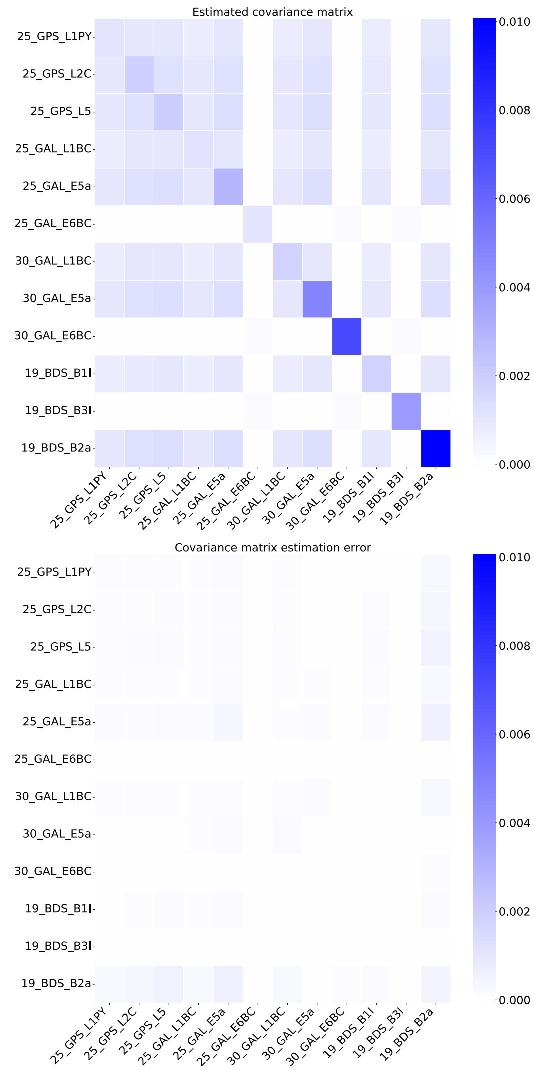

Fig. 9. Samples of covariance estimation results for the single-oscillator, zero-baseline experiment with the PolaRx5TR receiver.

B. Filtering Approaches

The differential phase between the oscillators ($\psi_{uv,\mathrm{os}}$) in a multistatic system can be modeled as follows:

$$\psi_{uv,\mathrm{os}}(t) = 2\pi \cdot f_{uv} \cdot t + \phi_{uv}(t) + \phi_0 \tag{13}$$

where f_{uv} is a frequency offset, ϕ_0 is a constant phase, and $\phi_{uv}(t)$ is a random phase error. The component $\phi_{uv}(t)$ can be further described as a stationary random process with the two-sided power spectral density (PSD) given by the composite power law as follows [30]:

$$S_\phi(f) = \frac{a_4}{f^4} + \frac{a_3}{f^3} + \frac{a_2}{f^2} + \frac{a_1}{f} + a_0 \tag{14}$$

where a_4 describes the random walk frequency noise, a_3 is the frequency flicker noise, a_2 is the white frequency noise, a_1 describes the flicker phase noise, and a_0 describes the white phase noise.

Assume that due to the short duration of SAR data acquisition and the proximity of the noise to the carrier, the $1/f^2$ component of the phase noise will dominate the measurements. Under these conditions, the baseband phase noise can be effectively modeled as a random walk, corresponding to integrating a Gaussian noise process. Based on this assumption, a Kalman filter can be developed using the simple model as follows:

$$x_k = \psi_{uv,0}[k] - 2\pi \cdot k \cdot \Delta t \cdot f_{uv} \tag{15}$$

$$x_k = x_{k-1} + w_k \tag{16}$$

$$z_k = \tilde{\psi}_{uv,0}[k] - 2\pi \cdot k \cdot \Delta t \cdot \tilde{f}_{uv} = x_k + v_k \tag{17}$$

where $\tilde{f}_{uv}$ is the frequency offset estimated through least-squares linear regression, Δt is the sampling period, x_k is the Kalman filter state variable, z_k is the measurement, $w_k \sim \mathcal{N}(0, q)$, and $v_k \sim \mathcal{N}(0, r)$ are the process and measurement noise, respectively. The variance q can be derived from the stability specifications of the oscillator in the time domain or calculated from direct phase difference measurements between oscillators of the same model in a controlled environment. The variance r can be determined from the single-oscillator, zero-baseline experiment described previously.

The filter described above was used throughout this article and demonstrated significantly better performance than the simple moving average filter. However, this model is not universally applicable to every oscillator, as, in some cases, other terms such as the frequency flicker ($1/f^3$ term) may dominate [31]. Nevertheless, this approach could still be effective as an empirical filtering method for other scenarios. A comprehensive evaluation of filtering techniques suitable for various types of oscillators is beyond the scope of this article.

Alternatively, or in addition to Kalman filters, empirically tuned least-squares smoothing could be used. Irrespective of the filter used, the power of error components—mainly oscillator tracking error and multipath—limits the effectiveness of a filtering approach in the same bandwidth as the legitimate phase noise signatures originating from the oscillators. Therefore, the more concentrated the oscillator power is around the main frequency, the more errors we can eliminate through filtering. In this sense, the high short-term stability required for radar payloads will favor the error budget of the GNSS-based technique presented here. In the end, the error budget for a specific system will depend mainly on the phase noise signatures of the oscillators, how successful the multipath isolation and/or suppression is, and the phase-noise characteristics of the main oscillator.

V. Experimental Results

A. Single-Oscillator Zero Baseline

Figs. 10 and 11 present the scaled and unbiased individual carrier phase measurement observables, as defined in (2), for a single-oscillator, zero-baseline experiment conducted using the OEM729 and PolaRxTR receivers, respectively. In this setup, the baseline components are effectively canceled, and the differential clock is nominally zero. As a result, the signals depicted in these figures provide a direct representation of phase noise estimation errors in the individual observables.

Both signals exhibit characteristics of colored noise, with the PolaRxTR showing a significantly lower noise level compared to the OEM729. Analyzing the 10-s time scale in

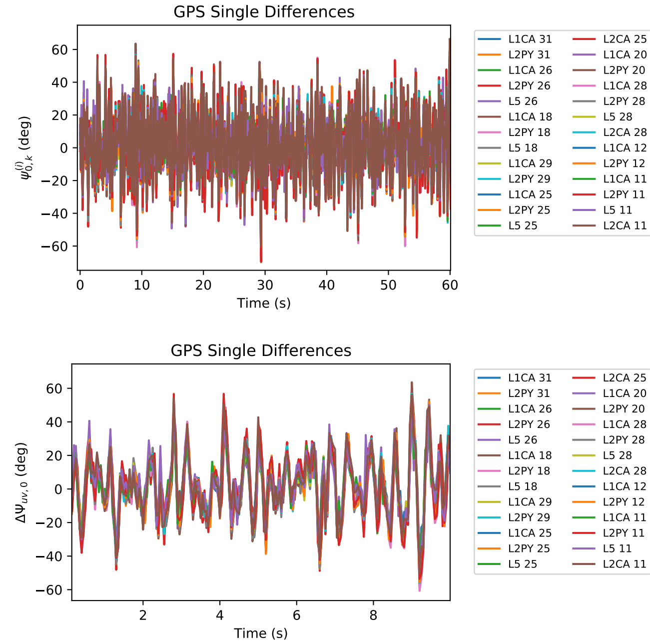

Fig. 10. Carrier phase single differences scaled to reference 5.4-GHz radar frequency for single-oscillator, zero-baseline experiment with the OEM729 receiver in two time scales.

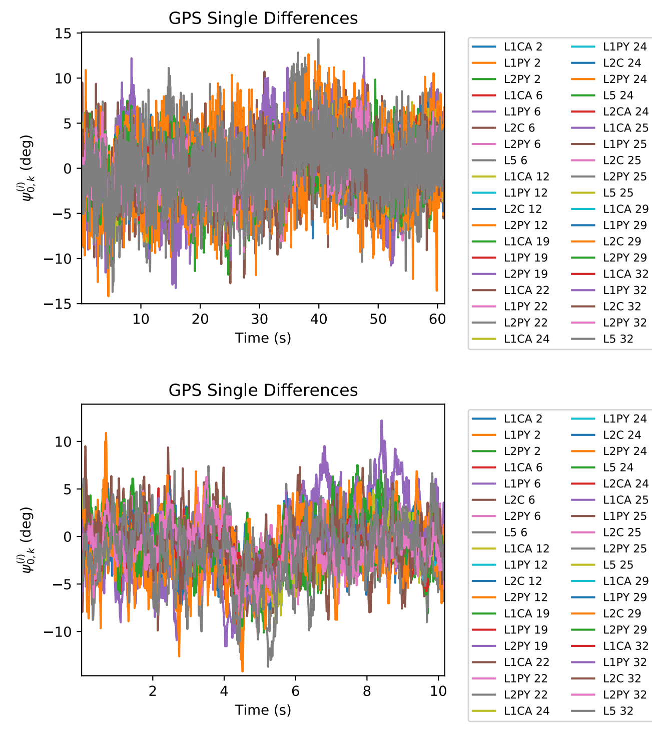

Fig. 11. Carrier phase single differences scaled to reference 5.4-GHz radar frequency for the single-oscillator, zero-baseline experiment with the PolaRx5TR receiver in two time scales.

Fig. 10 clearly reveals common contamination in the OEM729, which far exceeds its noise level. This contamination likely arises from disturbances in the clock path, environmental sensitivity, or phase noise introduced at the interface within the development kit.

When examining the short time scale in the zero-baseline results from PolaRx5TR shown in Fig. 11, we can see a slowly varying common mode although the error is dominated by a noise-like signal. The correlation between signals in the PolaRx5TR receiver is more clearly illustrated in Fig. 9, which depicts the correlation between differential phase estimation errors obtained from a common-oscillator, zero-baseline experiment. The figure reveals that for this receiver, the correlation depends primarily on the signal type and is largely independent of the originating GNSS satellite. Notably, Galileo E6 and Beidou B3 exhibit minimal correlation with all other signals, even those from satellites within the same frequency band. The presence of uncorrelated signals indicates the absence of common hardware contamination in the receiver clock interfaces and front end, as well as a lack of influence from local rapid atmospheric fluctuations.

In operational scenarios where antennas are separated and oscillators operate independently, this common mode cannot be identified directly from the carrier phase. It can only be mitigated through filtering and remains unaffected by averaging different carrier phase observables.

This result emphasizes that performance cannot be reliably predicted solely from noise specification. The phase tracking accuracy of the receiver must instead be determined experimentally. The simplest approach is to evaluate the covariance using the calibration procedure described in this article, which is based on the zero-baseline common-oscillator experiment. This experiment is straightforward to conduct, requiring only a pair of GNSS receivers under evaluation and no separate device for independent differential phase measurement.

It is important to note that both receivers exhibited a clear temperature sensitivity in data collected immediately after being powered on. Temperature variations introduce time-dependent delays in hardware components, leading to a common carrier phase drift. As mentioned above, environmental factors can also contribute to common mode effects. Therefore, for repeatable phase-tracking performance, it is essential that both receivers operate under thermally stable conditions, are properly isolated from environmental influences (in the case of a ground-based experiment), and are identically configured to minimize differences in thermal behavior.

B. Two-Oscillator, Zero Baseline

The main experimental results from the two-oscillator, zero-baseline experiments are shown in Fig. 12, scaled to the C-band (5.4 GHz), the L-band (1.2 GHz), and the X-band (9.8 GHz). The error signal for both receivers resembles filtered noise, showing no evident long-term drifts or systematic effects.

Fig. 13 shows the histograms of the synchronization errors when using the PolaRx5TRs for different processing steps applied. We can see that proper filtering and weighting based on characterizing the carrier phase measurements and oscillator phase noise largely improve the synchronization results. We see a reduction of standard deviation from 0.9° to 0.58° when applying optimal weights and an even greater reduction of the outliers, obtaining, in the end, a more symmetric and concentrated error distribution curve.

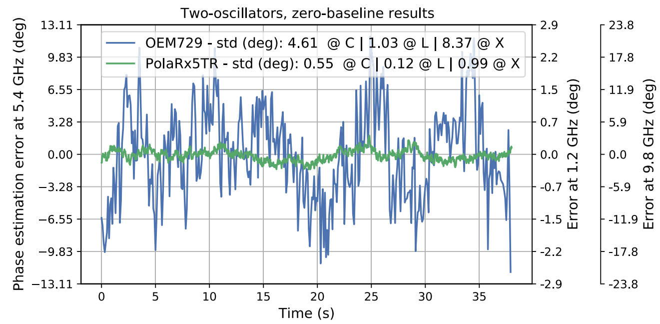

Fig. 12. Synchronization results for two-oscillator, zero-baseline experiment with the PolaRx5TR and OEM729 receivers. The standard deviation of the synchronization phase error at C-band equals 0.58° and 4.61°, respectively.

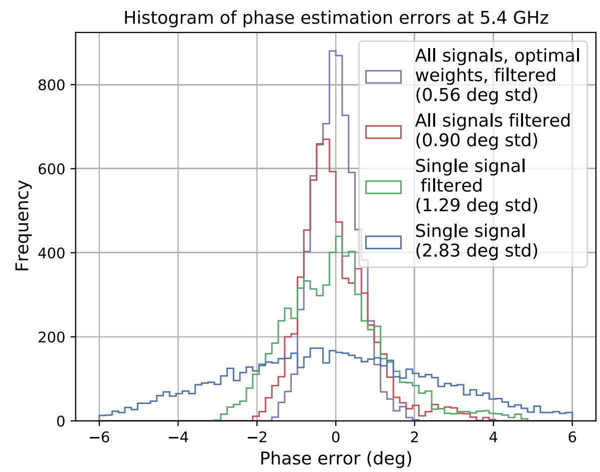

Fig. 13. Phase synchronization error histograms for different processing steps for a zero-baseline, two-oscillator experiment with PolaRx5TR receivers. The standard deviation of the synchronization phase error equals 1.29°.

In this experiment, external effects such as multipath and antenna phase center variations are canceled, leaving only noise and receiver contributions to affect the result, representing an optimistic scenario. The results were excellent for the PolaRx5TR in particular.

As a final remark, the performance results at different frequencies presented in Section V-B are derived from simple scaling. This approach implicitly assumes that the carrier generation at the radar payload does not introduce significant contamination from the oscillator to the output, or that any such contamination is calibrated, for instance, using a calibration loop. Designing the payload satisfying this condition is not trivial, and its difficulty might depend on the particularities of the mission payload and carrier frequency. Therefore, users of this technique must either impose this constraint as a design requirement or quantify and account for its contribution to the error budget. To satisfy this payload coherence maintenance requirement, high-quality and carefully tuned phase-locked loops (PLLs) and filters should be used for carrier generation. In addition, temperature drifts in the components along the payload chain, from the oscillator to the carrier generator, must be controlled or monitored and, if possible, compensated a posteriori.

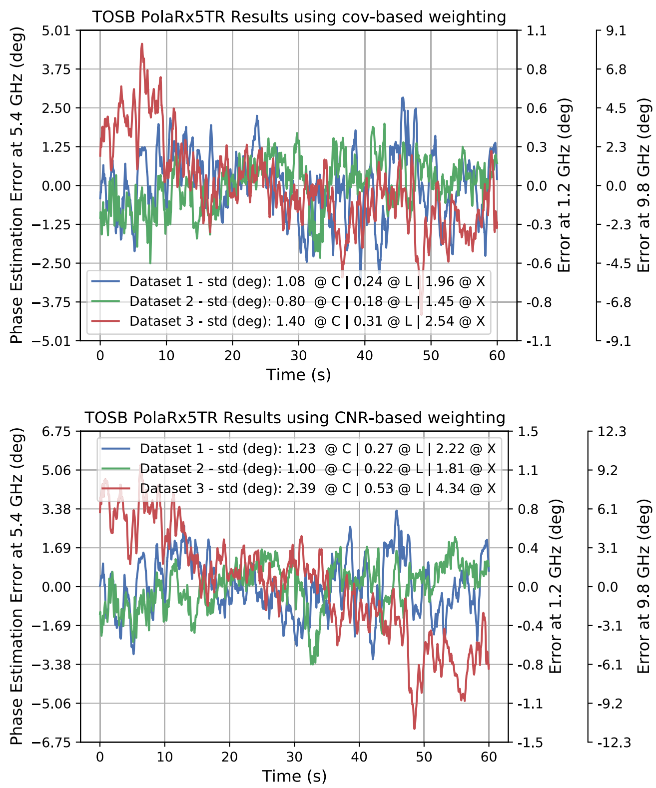

Fig. 14. Synchronization results for two oscillators in short-baseline experiments using the PolaRx5TR receiver. (Top) Weighting based on estimated covariances. (Bottom) Weighting based on measured CNR. Three datasets taken at different times and using different sets of GNSS satellites are shown.

C. Two-Oscillator Short Baseline

Fig. 14 shows the results from the two-oscillator, short-baseline experiment with the PolaRx5TR receiver. The figure shows three datasets taken at three different times and different sets of GNSS satellites in view. This experiment is the first assessment of the technique at the system level. Excluding the independent phase measurement setup, which would not be present in the real application, the two sets of reference oscillator, receiver, and antenna are completely physically disconnected and could be embedded on separate platforms. The two subplots correspond to the results using the weighting based on the carrier-to-noise ratio (CNR) estimated by the receiver, as suggested in [15], and using the estimated optimal weights with the covariance estimation method suggested in this article.

Compared to the zero-baseline experiments, the results reveal a pronounced increase in phase error, with the introduction of a slowly varying systematic error. The error, however, remains acceptable, particularly for L-band systems. This increase is most likely caused by multipath, given the proximity of the antennas to the ground and the lack of multipath suppression in the antenna hardware. It is worth noting, however, that in a spaceborne application, multipath interference is expected to be significantly lower, making the result in an operational scenario most likely between the one depicted in Fig. 12 and the one depicted in Fig. 14. This outcome depends on whether other error contributions—such as multipath, crosstalk, and the thermal environment—are effectively mitigated and assumes that no other previously unidentified factors are driving the results besides multipath.

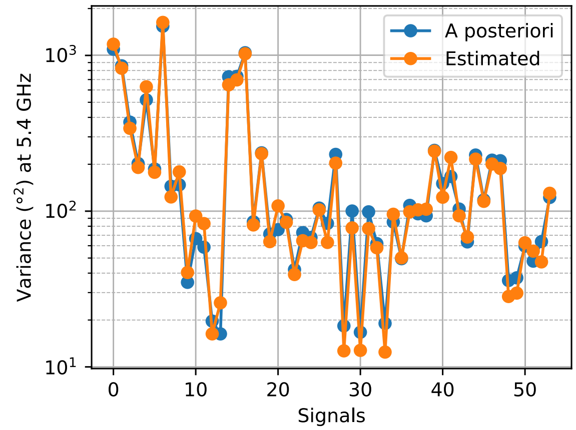

Fig. 15. Comparison between scaled carrier signals error variances measured a posteriori and the variances estimated, taken from a short-baseline and two-oscillator experiment with the PolaRx5TR.

When comparing the results of the weighting methods, it becomes clear that using estimated covariances yields significantly better outcomes. However, the improvement is less pronounced compared to the optimal weighting observed in the zero-baseline experiment shown in Fig. 13. This is because, in this case, multipath effects dominate the error budget, exerting a far greater influence than receiver contamination. The latter is the primary factor mitigated by assigning higher weights to signals unaffected by the common mode.

Fig. 15 compares the variances from the short-baseline experiment using the PolaRx5TR, calculated a posteriori and estimated. The figure demonstrates a good agreement between the a posteriori error variances and the estimated ones. It also reveals that some signals in the physical setup are affected by errors several orders of magnitude higher than expected from simple thermal noise, corroborating with the hypothesis of the results being driven by multipath interference. This plot also helps to understand the degraded performance. We see that many signals are heavily affected by multipath so that they are assigned a very low weight, and in practice, much fewer signals are used in the estimation. This estimation can be used also to reliably identify and exclude bad measurements by only comparing the carrier phase observables, without relying on external data.

Despite the severe multipath effect in most of the carrier phase observables, the algorithm successfully identified and assigned lower weights to the more affected measurements, achieving performance degradation but still comparable to the zero-baseline experiments. These results demonstrate the robustness of the technique against multipath effects and its effectiveness in assessing errors in individual carrier-phase observables under such conditions.

Fig. 16 presents the results of the short-baseline, two-oscillator experiments conducted with the PODRIX receiver in a simulated formation-flying scenario using a GNSS signal simulator. The upper plot shows the detrended phase noise estimates at the 5.4-GHz reference frequency and the detrended reference obtained through the direct phase

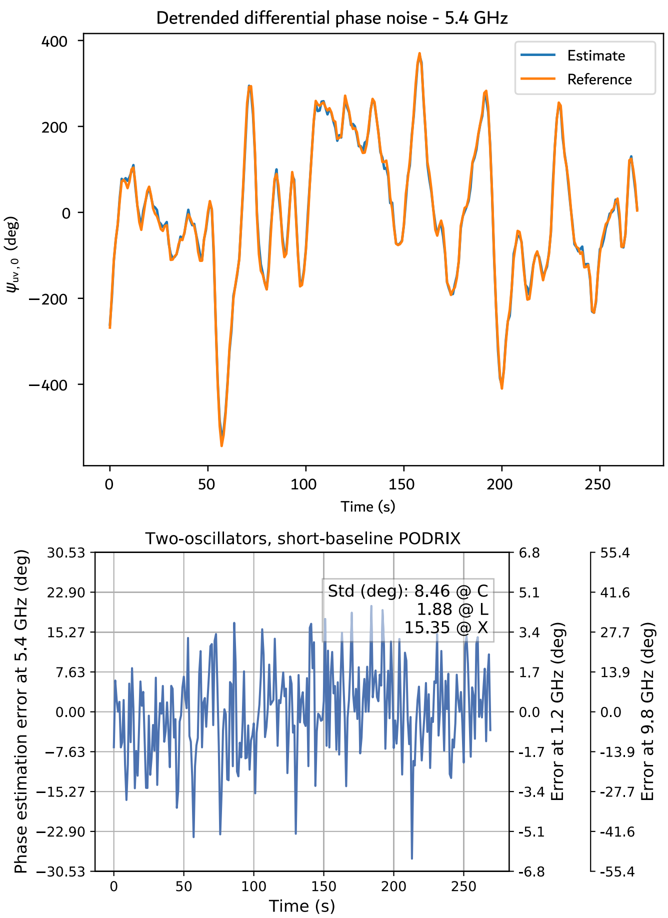

Fig. 16. Synchronization results for two-oscillator, simulated formation flying experiment with the PODRIX. Due to setup limitations, only L1 and E1 signals were used, and the sampling rate was limited to 1 Hz. The standard deviation of the synchronization phase error equals 8.46 degrees. The upper plot was detrended to facilitate visualization.

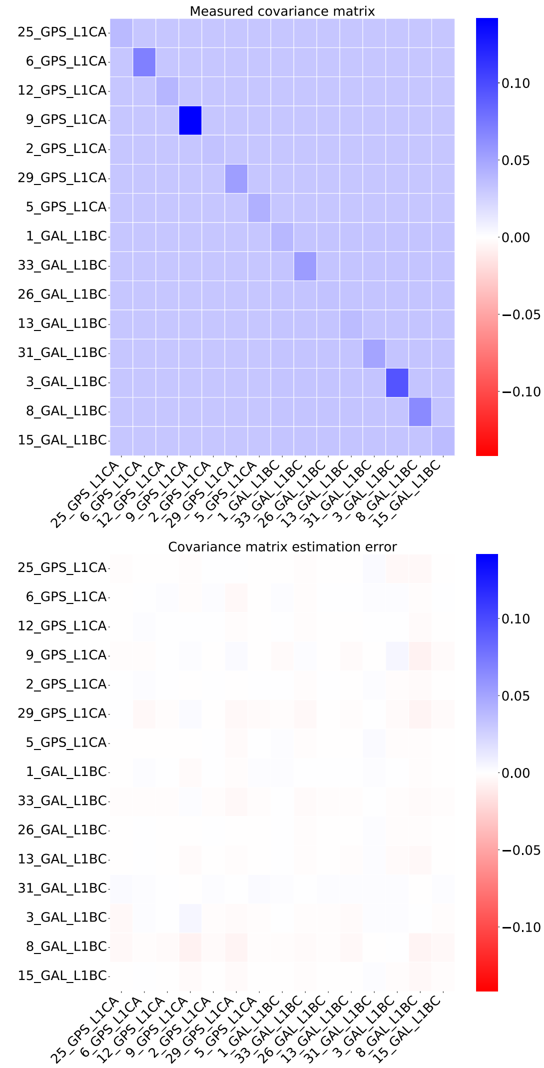

Fig. 17. Samples of covariance estimation results for the two-oscillator, short-baseline experiment with the PODRIX receiver.

measurement device. We eliminated the linear component to facilitate visualization, but note that the residual frequency is estimated seamlessly along with the phase noise by the algorithm. The lower plot illustrates the corresponding total differential phase error, including the estimated frequency offset, at different reference frequencies. Similar to the zero-baseline scenario, no distinctive systematic effects are observed.

The results in Fig. 16 demonstrate effective motion compensation, as the relative motion contribution—a dominant factor in formation-flying scenarios—was practically eliminated, yielding an estimated differential phase noise that closely matches the reference.

However, the synchronization phase error obtained (8.46°) was considerably higher than that of the PolaRx5TR. This discrepancy is at least partially attributable to differences in test conditions. In all experiments involving the PODRIX receiver, the carrier phase measurement update rate was fixed at 1 Hz due to limitations in the experimental setup. This low sampling rate may not only be insufficient to capture the differential phase noise spectrum, leading to interpolation errors, but also limits the potential for filtering improvements. In addition, only the L1 band could be simulated in the formation-flying scenario, reducing the number of signals available for averaging.

Fig. 17 shows the measured covariance matrix between signals in the formation-flying scenario with the PODRIX receiver, along with the error compared to the estimated matrix obtained by calibrating the off-diagonal terms in a zero-baseline experiment with a common oscillator, as described in Section IV. The individual errors were measured by scaling the carrier phase single-difference observables and compensating for the relative motion, followed by subtracting the measured differential phase drift. Using these errors, we directly estimated the covariance matrix.

The excellent agreement between the estimated and calculated covariance matrices reinforces the effectiveness of the proposed algorithm. More importantly, it demonstrates that the high Doppler difference between receivers in a formation-flying scenario does not significantly amplify the critical common-mode component, which could invalidate the concept if that were the case. This experiment provides an important verification of the technique's validity for orbital scenarios.

In conclusion, the test was successful as a proof of concept for an orbital scenario. However, determining the PODRIX receivers' final performance for this application would require an improved test setup. A higher sampling rate and a multiband GNSS antenna in a zero-baseline setup would be needed to characterize the covariance between all the different signals. This would allow us to verify the achievable noise reduction through point-by-point averaging and filtering.

VI. Conclusion

The proof of concept of the GNSS-based phase synchronization conducted in this study was successful. To the authors' knowledge, this is the first time that a GNSS-based synchronization experiment with a specially designed calibration and filtering approach has been shown to be accurate enough for a bistatic or multistatic SAR mission, with a synchronization phase error as low as 0.8° at the C-band for a short-baseline experiment with two oscillators. The precision achieved by the technique depends, however, on several factors. The main performance drivers identified in the experiment were the reference tracking precision of the receiver and multipath suppression. Through experiments, we discovered that the accuracy of the technique can be increased considerably by appropriate inspection of the signals, calibration of the covariance matrix of the measurement, and appropriate filtering.

The results show that the GNSS-based synchronization has the potential to be a simple and scalable solution for bistatic and multistatic SAR systems, which could guarantee compatibility of different systems designed and launched completely independently, opening many possibilities for data combinations across missions operating in the same band. They show that current technology could potentially achieve sufficient accuracy up to the C-band and hint at the potential of applicability to systems up to the X-band with incremental changes or the use of better-performing devices, as long as the previously identified main error contributions, such as multipath and crosstalk, are either suppressed or mitigated.

Finally, an important general conclusion drawn from the experiments is that the performance can be improved through precautions in the receiver design to prevent clock path contamination and potentially through adjustments in the configuration of the tracked signals.

Acknowledgment

The authors would like to thank Laura Agazzi and Steffen Thöllert from the Institute of Communications and Navigation, German Aerospace Center (DLR), Oberpfaffenhofen, Weßling, Germany, for their support with equipment and expertise for this project. They also thank Thomas Burger from ESA/ESTEC, Noordwijk, The Netherlands, for his support and valuable recommendations. Finally, they also would like to thank Heinz Reichinger from Beyond Gravity, Vienna, Austria, for his valuable input and support during the experiments.

References

[1] N. Sakar, M. Rodriguez-Cassola, P. Prats-Iraola, and A. Moreira, "Azimuth reconstruction algorithm for multistatic SAR formations with large along-track baselines," *IEEE Trans. Geosci. Remote Sens.*, vol. 58, no. 3, pp. 1931–1940, Mar. 2020.

[2] M. Grasso, A. Renga, G. Fasano, M. D. Graziano, M. Grassi, and A. Moccia, "Design of an end-to-end demonstration mission of a formation-flying synthetic aperture radar (FF-SAR) based on microsatellites," *Adv. Space Res.*, vol. 67, no. 11, pp. 3909–3923, Jun. 2021.

[3] G. Krieger and A. Moreira, "Spaceborne bi- and multistatic synthetic aperture radar: Potential and challenges," *IEE Proc. Radar Sonar Navig.*, vol. 153, no. 3, pp. 184–198, Jun. 2006.

[4] M. Kleinherenbrink, P. López-Dekker, F. Nouguier, and B. Chapron, "Bistatic SAR mapping of ocean-wave spectra," *IEEE Trans. Geosci. Remote Sens.*, vol. 62, pp. 1–12, 2024, Art. no. 4205812, doi: 10.1109/TGRS.2024.3394245.

[5] A. Moreira et al., "Tandem-L: A highly innovative bistatic SAR mission for global observation of dynamic processes on the earth's surface," *IEEE Geosci. Remote Sens. Mag.*, vol. 3, no. 2, pp. 8–23, Jun. 2015.

[6] G. Krieger, H. Fiedler, I. Hajnsek, M. Eineder, M. Werner, and A. Moreira, "TanDEM-X: Mission concept and performance analysis," in *Proc. IEEE Int. Geosci. Remote Sens. Symp. (IGARSS)*, vol. 7, Jul. 2005, pp. 4890–4893.

[7] M. Zink et al., "TanDEM-X: 10 years of formation flying bistatic SAR interferometry," *IEEE J. Sel. Topics Appl. Earth Observ. Remote Sens.*, vol. 14, pp. 3546–3565, 2021.

[8] G. Krieger et al., "TanDEM-X: A satellite formation for high-resolution SAR interferometry," *IEEE Trans. Geosci. Remote Sens.*, vol. 45, no. 11, pp. 3317–3341, Nov. 2007.

[9] J. Mou et al., "Interferometric calibration model for the LuTan-1 mission: Enhancing digital elevation model accuracy," *Remote Sens.*, vol. 16, no. 13, p. 2306, Jun. 2024.

[10] G. Krieger et al., "TanDEM-X: A radar interferometer with two formation-flying satellites," *Acta Astronautica*, vol. 89, pp. 83–98, Aug. 2013.

[11] G. Jin et al., "An advanced phase synchronization scheme for LT-1," *IEEE Trans. Geosci. Remote Sens.*, vol. 58, no. 3, pp. 1735–1746, Mar. 2020.

[12] M. A. Lombardi, L. M. Nelson, A. N. Novick, and V. S. Zhang, "Time and frequency measurements using the global positioning system (GPS)," *Cal Lab, Int. J. Metrol.*, vol. 8, pp. 26–33, Jan. 2001.

[13] W.-Q. Wang, "GPS-based time & phase synchronization processing for distributed SAR," *IEEE Trans. Aerosp. Electron. Syst.*, vol. 45, no. 3, pp. 1040–1051, Jul. 2009.

[14] J. S. Sandenbergh, "Synchronising coherent networked radar using low-cost GPS-disciplined oscillators," Ph.D. dissertation, Dept. Elect. Eng., Univ. Cape Town, Cape Town, South Africa, 2019.

[15] E. Rodrigues-Silva, M. Rodriguez-Cassola, G. Krieger, and A. Moreira, "GNSS-based phase synchronization for bistatic and multistatic synthetic aperture radar," *IEEE Trans. Geosci. Remote Sens.*, vol. 62, pp. 1–14, 2024, Art. no. 5213614, doi: 10.1109/TGRS.2024.3406797.

[16] J. L. Dekker et al., "The Harmony mission: Applications and preliminary performance," in *Proc. 6th Workshop Adv. RF Sensors Remote Sens. Instrum. (ARSI)*, 2019, pp. 1–6.

[17] P. López-Dekker et al., "The harmony mission: End of phase-0 science overview," in *Proc. IEEE Int. Geosci. Remote Sens. Symp. (IGARSS)*, Jul. 2021, pp. 7752–7755.

[18] P. van Barneveld, "Orbit determination of satellite formations," Ph.D. dissertation, Fac. Aerosp. Eng., Dept. Space Eng., Delft Univ. Technol., Delft, The, Netherlands, 2012.

[19] O. Montenbruck, P. Steigenberger, and A. Hauschild, "Broadcast versus precise ephemerides: A multi-GNSS perspective," *GPS Solutions*, vol. 19, no. 2, pp. 321–333, Apr. 2015.

[20] U. Weinbach, S. Schon, and T. Feldmann, "Evaluation of state-of-the-art geodetic GPS receivers for frequency comparisons," in *Proc. IEEE Int. Freq. Control Symp. Joint With 22nd Eur. Freq. Time Forum*, Apr. 2009, pp. 263–268.

[21] S. Sun et al., "POD performance of LEO satellites with Galileo high accuracy service (HAS) of initial service phase," *Adv. Space Res.*, vol. 75, no. 6, pp. 4963–4976, Mar. 2025.

[22] NovAtel. (Jul. 2023). *OEM729 Product Sheet*. [Online]. Available: https://hexagondownloads.blob.core.windows.net/public/Novatel/assets/Documents/Papers/OEM729-Product-Sheet/OEM729-Product-Sheet.pdf

[23] Septentrio. (2024). *PolaRxTR Product Sheet*. [Online]. Available: https://www.septentrio.com/en/products/gnss-receivers/gnss-reference-receivers/polarx-5tr#resources

[24] D. Calliess, O. Montenbruck, M. Wermuth, and H. Reichinger, "Long-term analysis of sentinel-6A orbit determination: Insights from three years of flight data," *Adv. Space Res.*, vol. 74, no. 7, pp. 3011–3027, Oct. 2024.

[25] F. Kunzi and O. Montenbruck, "Precise onboard time synchronization for LEO satellites," *NAVIGATION, J. Inst. Navigat.*, vol. 69, no. 3, 2022, Art. no. navi.531.

[26] F. S. Prol et al., "Position, navigation, and timing (PNT) through low earth orbit (LEO) satellites: A survey on current status, challenges, and opportunities," *IEEE Access*, vol. 10, pp. 83971–84002, 2022.

[27] L. Ai, W. Zhang, B. Zhong, F. Wang, X. Gong, and R. Zhang, "Hardware-in-the-loop simulation of real-time precise orbit determination for differential InSAR satellites using BDS-3 B1C/B2a measurements," in *Proc. China Satell. Navigat. Conf. (CSNC)*. Singapore: Springer, Jan. 2021, pp. 570–583.

[28] H. Cui and S. Zhang, "Satellite availability and service performance evaluation for next-generation GNSS, RNSS and LEO augmentation constellation," *Remote Sens.*, vol. 13, no. 18, p. 3698, Sep. 2021.

[29] M. Rodriguez-Cassola, P. Prats-Iraola, P. Lopez-Dekker, A. Reigber, G. Krieger, and A. Moreira, "Autonomous time and phase calibration of spaceborne bistatic SAR systems," in *Proc. 10th Eur. Conf. Synth. Aperture Radar*, Jun. 2014, pp. 1–4.

[30] J. Rutman, "Characterization of phase and frequency instabilities in precision frequency sources: Fifteen years of progress," *Proc. IEEE*, vol. 66, no. 9, pp. 1048–1075, Sep. 1978.

[31] E. Loria, S. Prager, I. Seker, R. Ahmed, B. Hawkins, and M. Lavalle, "Modeling the effects of oscillator phase noise and synchronization on multistatic SAR tomography," *IEEE Trans. Geosci. Remote Sens.*, vol. 61, pp. 1–12, 2023, Art. no. 5204212, doi: 10.1109/TGRS.2023.3249637.